Engineering Structures 227 (2021) 111413

Contents lists available at ScienceDirect

Engineering Structures

journal homepage: www.elsevier.com/locate/engstruct

Post-earthquake damage identification of an RC school building in Nepal using ambient vibration and point cloud data

Mehdi M. Akhlaghi [a], Supratik Bose [b], M. Ebrahim Mohammadi [c], Babak Moaveni [a,*], Andreas Stavridis [b], Richard L. Wood [c]

[a] Dept. of Civil and Environmental Engineering, Tufts University, Medford, MA, USA
[b] Dept. of Civil, Structural and Environmental Engineering, University at Buffalo, Buffalo, NY, USA
[c] Dept. of Civil and Environmental Engineering, University of Nebraska–Lincoln, Lincoln, NE, USA

ARTICLE INFO

Keywords:
Finite element model updating
System identification
Bayesian inference
Structural health monitoring
Damage identification
Lidar point clouds
Gorkha earthquake

ABSTRACT

This paper presents a damage identification and performance assessment study of a four-story masonry-infilled reinforced concrete building in Sankhu, Nepal, using ambient vibration and point cloud data measurements. The building was severely damaged during the 2015 Gorkha earthquake. A set of accelerometers was used to record the ambient response of the building in order to extract its modal parameters, and a series of lidar scans were collected to estimate the surface defects of certain structural components. An initial model of the structure is created using a recently proposed strut model for masonry infills and a novel modeling approach for infilled RC frames. Dimensions are extracted from lidar-derived point cloud data in the absence of as-built drawings. The FE model updating is first performed through a deterministic formulation where optimal model parameters are estimated through a least squares optimization, and then through a Bayesian inference formulation where the joint posterior probability distribution of the updating parameters are estimated based on the prior knowledge of updating parameters and likelihood of measured data. The error functions for both formulations are defined as the difference between identified and model-predicted modal parameters. Two cases of model updating are performed using different parameterizations and different prior information about the damage. In the first case, updating parameters include walls and columns along the four stories of the building and exclude structural components observed to be severely damaged. The prior knowledge about structural component stiffness values is based on the expected material properties. In the second case of model updating, updating parameters include walls and columns of only the first story, and the prior stiffness values are estimated from the point-cloud measurements. The prior values are then updated using the vibration measurements. The damage identification results are in good agreement with visual observations and point cloud damage quantifications. The most probable model parameters in the Bayesian approach are also found to be in good agreement with the optimal results obtained in the deterministic formulation. Finally, it is shown that the probabilistic natural frequency predictions provide more realistic confidence bounds when both modeling errors and parameter uncertainties are accounted for in the prediction process.

1. Introduction

Assessing the condition of existing structures is a major challenge after the occurrence of strong earthquakes. Visual inspections carried out by experienced engineers are usually the most common approach for the safety assessment of structures. While these inspections provide an effective way of estimating the damage severity for buildings, they can be inefficient and subjective in identifying damaged areas [1]. In order to overcome this shortcoming, destructive and nondestructive methods have been proposed to supplement visual inspections for performance assessment of structures.

Among the suggested nondestructive post-earthquake assessment methods, vibration-based damage identification methods have gained more attention in the last two decades, and researchers have used vibration measurements to identify the location and severity of the damage in buildings and bridges. Huang et al. [2] used a set of measured acceleration responses along with the base excitation recordings to train a neural network framework for response assessment of a five-story steel

* Corresponding author.

https://doi.org/10.1016/j.engstruct.2020.111413
Received 28 October 2019; Received in revised form 27 July 2020; Accepted 5 October 2020
Available online 28 October 2020

frame building damaged through different intensities of the Kobe earthquake simulated using a shake table. A full-scale seven-story RC structure was built and tested on the UCSD-NEES shake table, and its performance was evaluated at different levels of induced damage with the help of vibration recordings [3].

Finite element models of structures are commonly used to predict the behavior of structures and assess their performance. However, these models are more effective if they are calibrated with measured data to reduce the modeling errors caused by potential damage that may have occurred during the earthquake. There are different sources of error in the modeling of large-scale civil structures, some of which can be reduced through the calibration process, and with the help of experimental data. This includes errors related to erroneous assumptions about effective parameter values such as modulus of elasticity, mass or cross-sectional properties [4], and tuning them can compensate for other sources of modeling error to some extent. Overall, models can often accurately represent the measured data that are used in the calibration process.

Extensive efforts have been undertaken to develop, assess, and expand various model updating techniques, as summarized in seminal publications [5–7]. Model updating algorithms have been developed utilizing modal parameters such as natural frequency [8,9], mode shape [10,11], mode shape curvature [12], modal flexibility [13] and their combinations [14]. Despite the improvements in deterministically formulated model updating methods, they are still incapable of quantifying the uncertainties in the updating results. Modeling errors, as mentioned earlier, together with identification errors, measurement noise, and variability in ambient and environmental conditions would cause uncertainty in model updating results.

Probabilistic model updating methods, including those based on Bayesian inference, consider the modeling errors and measurement noise in the updating process [15,16]. Ching and Beck [17] and Yuen et al. [18] implemented Bayesian model updating approaches to the IASC-ASCE benchmark problem. Ching and Chen [19] developed the transitional Markov chain Monte Carlo (TMCMC) method to improve the efficiency of Bayesian model updating and address the challenges in sampling multimodal or very peaked posterior distributions. Zhang et al. [20] developed a Bayesian inference approach to consider different kinds of errors, including measurement noise, modeling errors, and effects of the linearity assumption. Sankararaman and Mahadevan [21] used Bayesian inference for detection, localization, and quantification of damage. Behmanesh and Moaveni [22] have used Bayesian model updating to estimate damage on a footbridge and quantify the value of added information on accuracy of the results. Jang and Smyth [23] proposed a sensitivity-based cluster analysis for the selection of updating parameters in the Bayesian model updating of a full-scale FE bridge model. Sun and Betti [24] proposed a hybrid optimization algorithm for probabilistic model updating using the sensitivity-based cluster analysis. The above-reviewed studies consider linear elastic structural models in the updating process. In contrast, many studies in the literature are focused on the identification of nonlinear structural systems through model updating. Song et al. [25] have proposed the use of nonlinear normal modes for identification of geometric nonlinearity while several other researchers have proposed the use of extended or unscented Kalman filters for identification of nonlinear material behavior [26 –30].

This paper studies the post-earthquake performance of a masonry-infilled RC building that is located in Sankhu, 13 km northeast of Kathmandu, and 87 km from the epicenter of a 7.8-magnitude shallow earthquake which struck Gorkha district in central Nepal [31,32]. The building was red-tagged by local engineers due to the extensive damage in walls and columns of the first story. Modal parameters of the building are extracted from the ambient vibration recordings, and a FE model of the building is developed with the help of lidar and experimental data using a novel modeling approach [33]. This model is then updated through a Bayesian model updating process, which gives both the most probable values and the variance of the updating model parameters. In addition, lidar point cloud data was collected to document condition of the structure, identify the building geometry accurately, and detect and quantify surface damage within structural elements. The estimated surface defects from lidar data are compared to the identified damage from vibration measurements. Finally, the effect of modeling errors on model-predicted natural frequencies is investigated.

The main novelty of this study includes the combination of state-of-the-art model updating and point-cloud analysis methods for damage identification using a unique set of in-situ measurements. These measurements were obtained from an actual building damaged by an earthquake and were used in parallel in the model updating process. This provides a unique opportunity to (a) compare and validate the identification results obtained from vibration and point-cloud measurements, (b) apply a novel modeling approach for RC buildings with masonry infills, (c) implement a probabilistic model prediction approach that accounts for modeling errors on an actual building with realistic earthquake damage, and (d) explore an approach for combining the ambient vibration measurements (in likelihood function) with the detected damage from the point cloud data (in prior distribution) in the model updating process.

2. Description of building

The four-story school building located in Sankhu, Nepal, has a masonry-infilled reinforced concrete frame. It has seven bays in the north–south direction and two bays in the east–west direction (Fig. 1.a). The west side of the building has a balcony in the first three stories serving as a corridor. The infill walls on the east side of the building have wide and relatively short windows, while in the middle of the building, the walls had larger windows and/or doors. As presented in the plan view of the building (Fig. 1.b), the staircase is located towards the north end, which induces torsional irregularity to the structure.

Major damage was observed in the structural components of the first story after Gorkha earthquake. The damage was concentrated towards the south end of the structure with shear failures in the columns (Fig. 2.a) and extensive damage in the beam-column joints (Fig. 2.b). This damage pattern can be attributed to the inadequate stirrups. The infill panels towards the south were separated from the bounding frames, and developed dominant horizontal and shear cracks (Fig. 2.c). However, the RC members and the infills towards the north of the structure were only slightly damaged. This non-uniformity in the distribution of damage can be attributed to the torsional irregularity introduced by the location of the staircase. The damage in the upper-story infill panels and RC columns were not significant. More information about the building can be found in [34].

3. Data collection and processing

3.1. Ambient vibration data

Data was collected in two instrumentation setups, with Setup A measuring ambient acceleration at the top three floors (3–5) and Setup B measuring it at the bottom three floors (1–3). Third floor accelerometers were kept in place for both setups and served as reference in identifying and combining the mode shapes. In Setup A, 45 min of acceleration data were recorded at the top three floors of the building, while 54 min of acceleration data were recorded for the bottom three floors in Setup B. Each floor was instrumented with 4 accelerometers placed in two opposite corners and along two perpendicular directions as demonstrated in Fig. 1.

The collected data is segmented in 9-minute intervals; resulting in five sets of acceleration data for Setup A and six sets of acceleration data for Setup B. Each of these 11 sets of data is filtered using a band-pass Finite Impulse Response (FIR) filter [35] of order 4096 for frequencies between 1 and 10 Hz. In order to improve the computational efficiency and without loss of accuracy, the filtered signals are down-sampled from

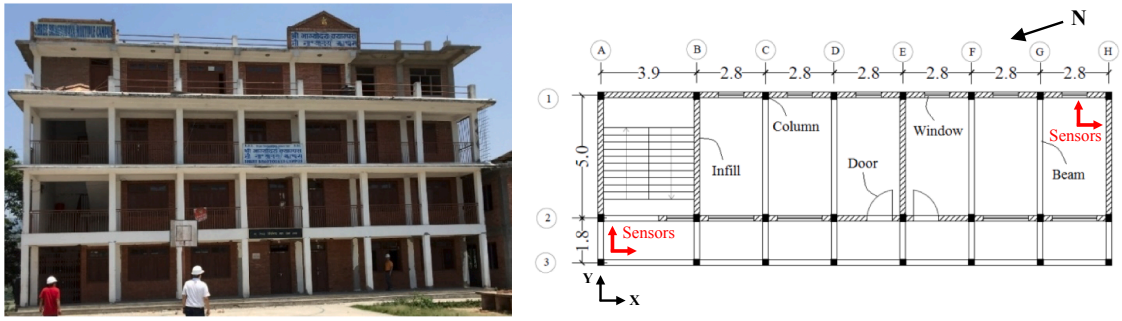

(a) elevation view (b) plan view and location of sensors

Fig. 1. Four-story school building (dimensions in meters).

(a) Column G2 (b) Column H1 (c) Infill wall H12

Fig. 2. Observed damages in the first story of the building.

the initial sampling rate of 2048 Hz to 256 Hz. Most of the channels in the north-west corner of the building (close to the staircase) have a high signal-to-noise ratio for the system identification process, leaving us with 11 channels to work with (out of the 20 total recorded channels). Fig. 3 shows the acceleration time history and the Fourier amplitude spectrum of the sensor at north-west corner of 3rd floor measuring in the north–south direction.

An output only method is used for the identification of modal parameters of the building. The Natural Excitation Technique [36,37] and the Eigensystem Realization Algorithm (NExT-ERA) [38] is used to identify the modal properties of the structure in the absence of input measurements. Eight equal length Hanning windows are used with a 50% overlap in computing the cross power spectral densities between the used acceleration channels and two reference channels. The inverse Fourier transform of these cross power spectral densities is calculated as an estimate for the free vibration response. Modal parameters of the building are then identified through singular value decomposition of an $(11 \times 400) \times (400 \times 2)$ Hankel matrix formed using the estimated free vibration response.

Stabilization diagrams, together with the power-spectral density (PSD) functions of measured accelerations, are used to find the stable and most excited vibration modes of the building. A stabilization diagram is demonstrated in Fig. 4 for one set of data together with the PSD of the reference channels considered. Four stable modes are observed below 6 Hz, where the identified natural frequencies remain stable with increasing model order. The first three modes with the highest energy (as indicated by peaks of the PSD and identified with lowest model order) are selected as the stable and most excited vibration modes of the building. It is worth noting that the mode at 5.4 Hz is also stable and identifiable from the data. However, due to the fact that contribution of this mode to response is minimal, we have not included this mode in the model updating process.

Similar system identification process is performed using different datasets in order to identify 11 sets of modal parameters. To assemble the mode shapes derived from the two setups, the mode shape values are normalized to the shared mode shape coordinates located at the third floor [39]. Table 1 shows the statistics of the identified natural frequencies and damping ratios.

Modal damping ratios are identified with larger COV than the natural frequencies for each setup and also show some deviation between the

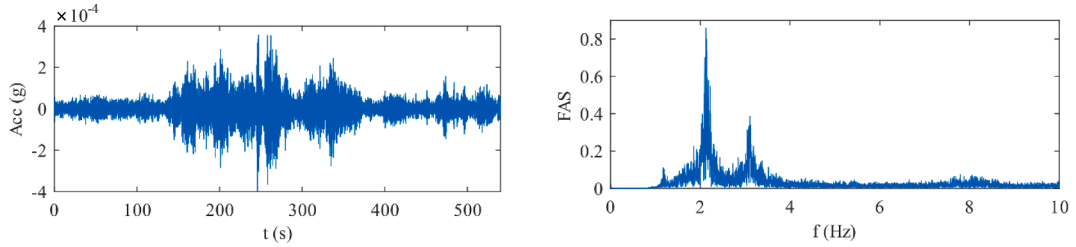

Fig. 3. Time history and Fourier spectrum of filtered and down-sampled acceleration measurement of the 3rd floor.

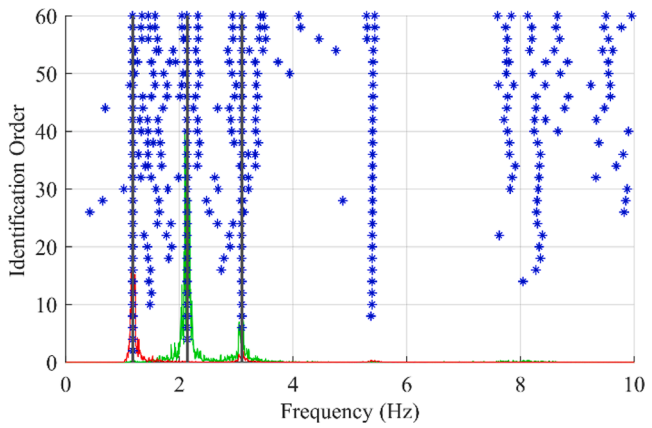

Fig. 4. A stabilization diagram and identified natural frequencies (vertical lines).

Table 1
Mean and coefficient-of-variation of identified natural frequencies and damping ratios.

Setup	Mode	Natural Frequency [Hz]		Damping Ratio [%]	
		Mean	COV [%]	Mean	COV [%]
A	1	1.19	0.6	2.2	15.3
	2	2.16	1.3	2.2	17.6
	3	3.14	0.9	3.0	36.2
B	1	1.20	0.5	1.8	32.5
	2	2.16	1.7	1.5	42.0
	3	3.18	0.8	2.4	18.4

two setup mean values. The average identified modal damping of 2.0%, 1.8%, and 2.7% for modes 1 to 3 are reasonable, but slightly larger than expected during very low amplitude ambient excitations, which may be due to the significant damage in the building.

3.2. Point cloud data

Numerous workflows have been proposed for analyzing point clouds to detect damage using intensity values or geometric properties of point normal vectors [40–42]. The use of digitized surface observations has also proven valuable to the engineering community in estimating member capacity [43]. In this study, a method based on Mohammadi et al. [44] is extended to investigate the damage severity for the masonry walls, which represent a more complicated problem due to their complex surface geometry. Point cloud datasets used within this study were captured by two ground-based lidar scanners [45]. Fig. 5 depicts the approximate locations of the 13 exterior scans. The scans were registered to a unified coordinate system via a cloud-to-cloud optimization for a point cloud of the entire structure through Faro Scene software. The aligned scans result in a mean registration accuracy of 2.7 mm for the entire dataset and less than 2 mm for walls and columns at the ground level.

Point clouds of the selected walls and columns are used to detect surface defects and identify the severity of damage in various structural components. The surface defect metrics are then compared to the identified loss of stiffness in various components from model updating results (similar to the work of Song et al. [46]). The algorithm developed to detect damaged areas of each wall or column uses two local geometric surface descriptors to evaluate the local variation of each point relative to its eight neighboring points. The algorithm initiates by downsampling the point cloud data through a voxelization process using a predefined voxel dimension (at the centimeter level), which results in a point cloud with reduced point density. Afterward, the sparse points are eliminated from the point cloud through a statistical outlier removal process. The first geometric surface descriptor used is the surface variation which is calculated for each point and its eight closest neighboring points, as shown below:

$$\gamma_n = \frac{\lambda_1}{\lambda_1 + \lambda_2 + \lambda_3} \tag{1}$$

where γ_n represents the surface variation value for point P_n and λ_1, λ_2, and λ_3 ($\lambda_1 < \lambda_2 < \lambda_3$) denote the eigenvalues of the covariance matrix for each point and its neighboring points [47]. The second geometric surface descriptor used within the method is the variation of normal vector at each point with respect to its local reference vector. The normal vector for each point is estimated through a weighted average method, known as mean weighted area of adjacent triangles (MWAAT) [47]. The normal vector is computed using MWAAT based on eight closest neighboring points, as shown below:

$$N_{MWAAT} = \sum_{i=1}^{8} \left(\frac{\vec{E}_i}{|E_i|} \times \frac{\vec{E}_{i+1}}{|E_{i+1}|} \right) |E_i \times E_{i+1}| \tag{2}$$

where E_i represents the edge between central point P and its i^{th} neighbor P_i, and $(\frac{\vec{E}_i}{|E_i|} \times \frac{\vec{E}_{i+1}}{|E_{i+1}|})$ is the unit normal vector of the i^{th} adjacent triangle with two edges of E_i and E_{i+1}. The local reference vector for each point is estimated based on eigendecomposition of the point and its 24 neighbors where the eigenvector corresponding to the smallest eigenvalue represents the local reference vector. Once the two surface descriptors are computed for each point, a probability distribution function for each

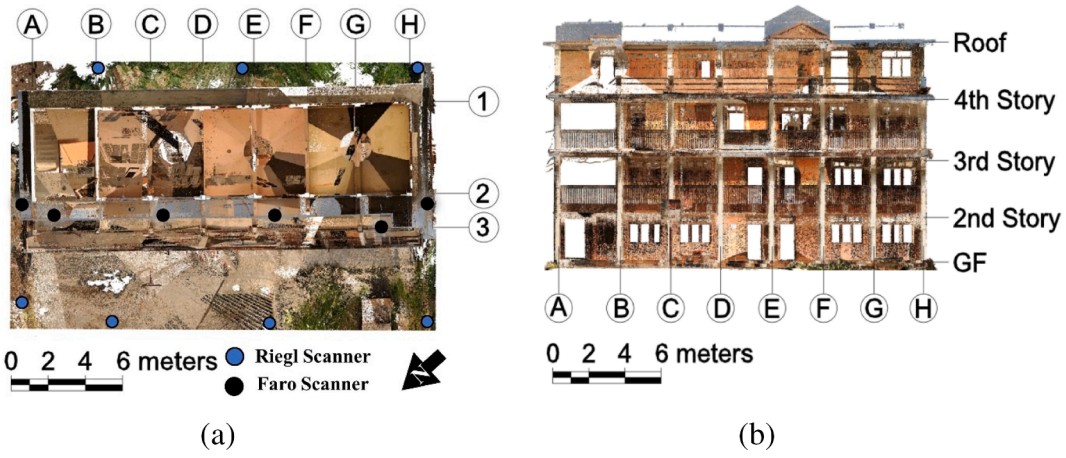

Fig. 5. Point cloud data: (a) top view of typical scanner placement for exterior scans and (b) elevation view of the structure.

surface descriptor is estimated through the Kernel probability distribution function (PDF), and a damage percentile is identified to classify the points into damaged and undamaged segments based on its signed curvature change. The damage percentiles within this study are estimated directly from the Kernel PDF. In the last step, damage detection algorithm compares the classification result based on each surface descriptor and reevaluates the classification of the points. In this step, each point is reclassified as damaged if and only if the point was classified as damaged by both surface descriptors. Therefore, the percent of surface damage can be computed in addition to the location of the damaged areas.

Within this study, the damage propagation in the structure is investigated through analysis of the various components, including the front columns, interior walls, and exterior walls. To analyze the selected point clouds, each dataset is initially subsampled to reduce the point density variation and resolution differences between each dataset. In this study, all three components are examined to provide a detailed and complete understanding of the damage evolution as imposed by the torsional response of the structure.

Columns: The columns at the front side of the structure are evaluated using the detection algorithm to quantify significant cracking, concrete spalling, and other surface defects. Within this study, the column point clouds were subsampled using a voxel dimension of 1 cm. Table 2 summarizes the surface defect percentage for each column and the type of damage observed.

It is observed that the columns close to the staircase sustained minor to moderate damage, including localized spalling at two sides or ends (values as low as 6%). On the other hand, the columns close to the southern side of the structure sustained moderate to significant spalling and exposed reinforcement, which indicates that the southern side of the structure developed more damage (values up to 40%).

Interior walls: The analysis of the interior scans is performed on three walls at the north, middle, and most southern portions of the structure, namely H12, E12, and B12 (see Fig. 1). The interior walls are subsampled using a voxel dimension of 2 cm to reduce any resolution differences between scans of different walls. Table 3 presents the summary of the surface defect percentage for each interior wall and the type of damage observed. Fig. 6 illustrates the damage classification for the interior walls. Within Fig. 6d, e, and f, the detected defects are shown in red (or gray in black and white prints), while the intact and undamaged surfaces are shown in black. As demonstrated, the interior wall B12 sustained the least damage during the event with an identified percent damage of 5%, as evidenced via a significant horizontal cracking at the center of the wall (Fig. 6a). However, both E12 and H12 walls demonstrated severe damage including significant spalling and considerable diagonal cracking (Fig. 6b and c). The percent defect identified for walls E12 and H12 are 23% and 22%, respectively. Note that the color variation between scans of walls B12, E12, and H12 is due to using two different lidar scanners during the data collection process. Moreover, the vertical white lines within the wall H12 is the result of occlusion due to steel shoring posts.

Table 2
Surface defect percentage values of selected columns in the first story.

Member ID	Surface Defect (%)	Description
A2	6	Minor surface defects and edge spalling on both faces
B2	26	Spalling of concrete cover at the edges, shear crack at the bottom
C2	29	Minor edge spalling on left, significant localized spalling on top right
D2	28	Shear cracks evident on top and bottom, edge spalling on both sides
E2	32	Shear cracks evident on top and bottom, edge spalling on both sides
F2	33	Shear cracks evident on top and bottom, edge spalling on both sides
G2	30	Shear cracks evident on top and bottom, edge spalling on both sides
H2	40	Significant spalling on top of both faces with exposed reinforcement, shear crack on the bottom

Table 3
Surface defect percentage values of interior walls in the first story.

Member ID	Corresponding Fig. 6	Surface Defect (%)	Description
B12	a, d, and g	5	Minor surface defects throughout and one significant horizontal cracking
E12	b, e, and h	23	Significant diagonal cracking and moderate to severe spalling
H12	c, f, and i	22	Significant diagonal cracking and severe spalling

Exterior walls: The damage evolution within the structure is assessed using data collected from the exterior walls. To achieve this objective, all the exterior walls on the first floor are analyzed except for walls CD1, EF1, and GH1, which are not analyzed due to occlusion from vegetation. The points are classified into likely damaged (damaged areas and sharp features) and undamaged classes. However, the detection algorithm classifies the sharp features (here brick boundaries) as potentially damaged areas, which reduces the accuracy of the computed damage percentile for this exposed masonry element. Therefore, to address this construction feature, the classified damaged points are further analyzed to quantify the damage severity. To achieve this goal and specific to this study, a best-fitted plane is identified for the undamaged classified points and used to further analyze the damaged classified vertices in terms of damage severity. To analyze the damaged vertices, the developed method quantifies the distance from the median value of each damaged point with respect to the best-fitted plane. These values are then binned into 2 mm intervals. The results binning process can quantify the severity of likely damaged areas, which represent the mortar loss or cracking. Fig. 7 depicts the result of damage severity analysis for the walls A12 and H12, as an example. As shown in Fig. 7b, severe cracking was observed within the exterior side of wall H12 with varying depth of 1.4 cm to 4 cm, while no significant damage detected within the exterior of wall A12 (Fig. 7a).

The developed method to assess the surface damage severity for the exterior masonry walls uses a singular damage metric. This contrasts with the columns and interior walls, which utilized percent area. For these exterior walls, each of the walls binned damage values are analyzed via a cumulative distribution function (CDF). The CDF permits a quantitative assessment through computing the area under the curve (AUC). CDF curves computed for the seven infill walls on the north side of the building (axis 2) are shown in Fig. 8. The higher values of AUC correspond to the smaller loss of grout or cracking within a brick masonry wall and vice versa. Note that the value of AUC directly corresponds to and quantifies the loss of grout and/or cracking within the walls for a quantitative comparison between similar elements.

To compare all the walls within the first floor quantitatively and study the damage propagation due to the event, the walls are classified based on the computed AUC of CDF curves. Fig. 9 represents the color-coded figure of walls organized based on the AUC values. Within Fig. 9, the red color corresponded to the lowest AUC values (most damaged), while the blue color corresponds to the highest AUC values (least damaged). As shown, the southern side of the structure sustained significantly more damage, which matches the observed damage propagation in the interior walls and columns.

The analysis results indicate that the structure only experienced minor to moderate spalling, cracking, and other surface defects near the stairwell on the north end of the building. In contrast, the south end of the structure experienced moderate to severe damage that may be explained by the torsional dominated response due to the stiffness irregularity created by the concrete stairs as well as the openings, doors,

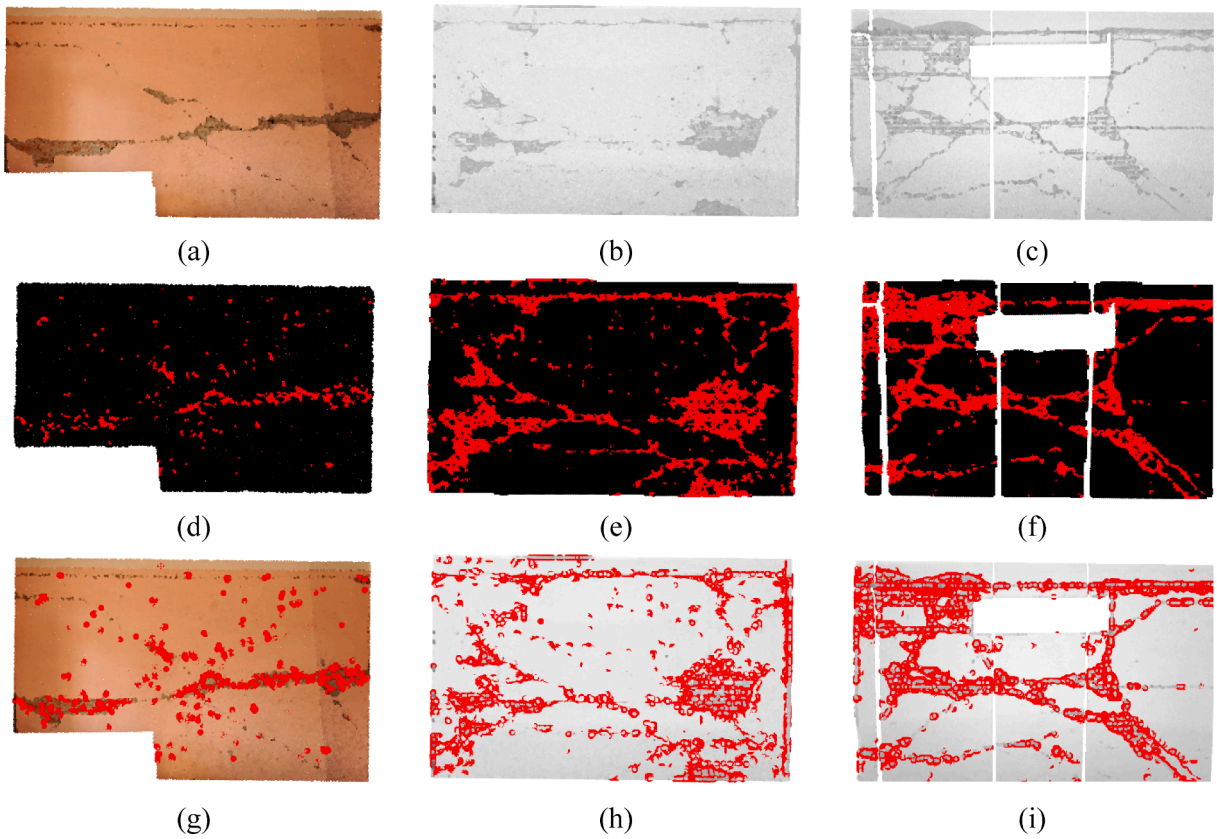

Fig. 6. Identified surface defect areas for interior wall: original RGB colored point cloud of (a) B12, original grayscale colored point cloud of (b) E12 and (c) H12, color-coded detections of (d) B12, (e) E12, and (f) H12, and superimposed detected defects to colored point cloud of (g) B12, (h) E12, and (i) H12.

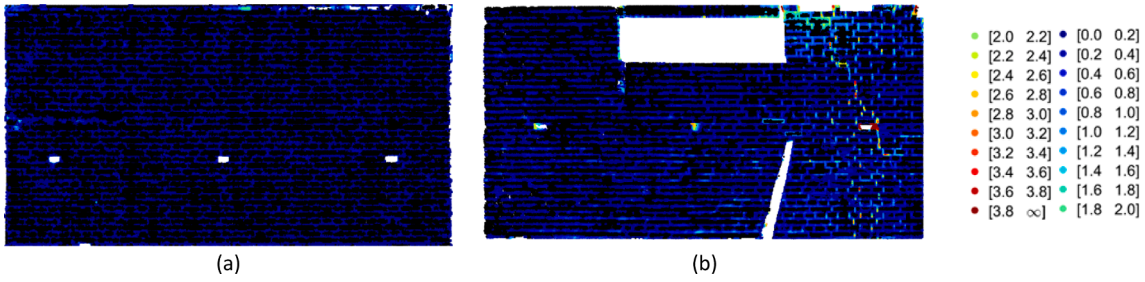

Fig. 7. Depth analysis (in cm) of detected defects for the exterior wall point clouds: (a) A12 and (b) H12.

and windows, within the walls, such as EF2 and DE2. This is based on the analysis of the interior and the exterior walls and the columns.

The developed methods to analyze point clouds reduce the subjectivity associated with traditional visual inspection methods as the damaged areas are detected primarily based on frequency analysis of overall surface local geometric variations. The local geometric variations are computed based on the spatial orientation of each point with respect to its neighboring vertices using identical procedures, guaranteeing consistency throughout the process. As a result, the developed method limits the subjectivity of visual inspection to the procedure used to collect point clouds data and its quality due to the direct human identification and quantitation of damage.

4. Finite element modeling

A finite element model of the school building at Sankhu has been developed in the structural analysis software, OpenSEES [48]. The geometry of the model is based on the analysis of point cloud data, which is complemented with *in situ* measurements. The material properties are assumed according to the tests reported in [49] in the absence of actual test data. The compressive strength is considered to be 9.65 MPa for concrete and 3.45 MPa for masonry, while the elastic moduli are 13940 MPa and 2550 MPa for concrete and masonry, respectively. Based on recommendations of ACI [50], the initial stiffness of concrete elements is assumed to be 40% of the analytically estimated stiffness, to account for the potential deterioration of the structure prior to the earthquake.

The numerical model is developed following the methodology proposed in Bose et al. [51]. It adopts displacement-based inelastic beam-column elements [52] for the RC members, and truss elements for the diagonal struts representing the infill. Each infilled bay is classified according to the anticipated failure pattern, and the backbone curve for the infilled bay is derived using simple analytical equations following the methodology proposed by Martin and Stavridis [53,54] for frames with solid infills, now adopted in ASCE 41–17 [55].

Once the lateral force vs. displacement curves are developed, the struts are calibrated so that when added to the model of the bare single-bay RC frame, the combined response matches the analytically derived backbone curve. The numerical model of the entire building, consisting

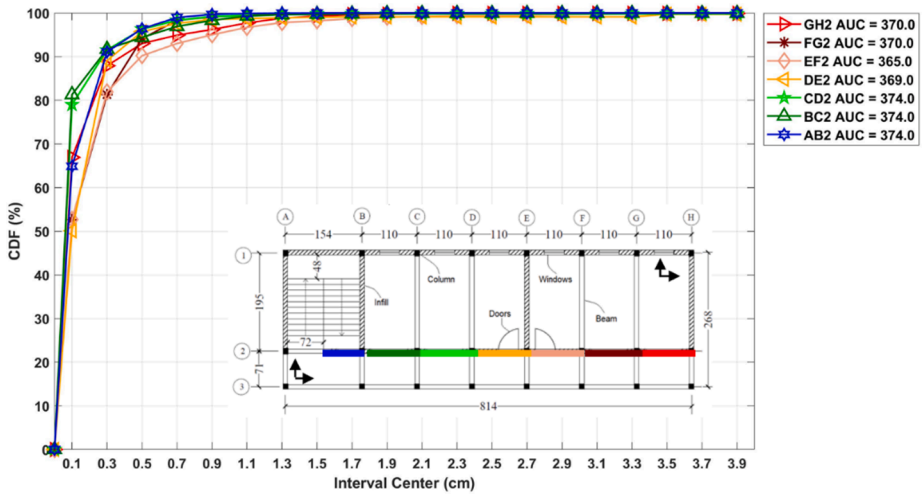

Fig. 8. Typical computed CDF curves for the northern walls.

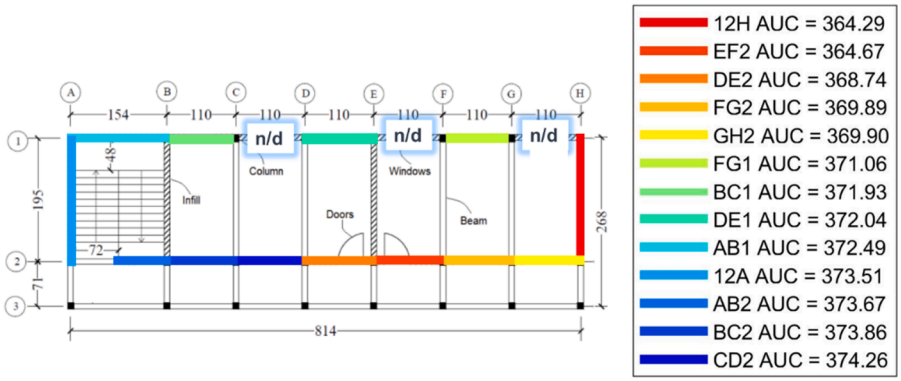

Fig. 9. Color-coded walls based on AUC of CDF curve.

of 428 elements, is then assembled (Fig. 10). The nonlinear model is used to simulate the performance of the actual building when subjected to the nearby recorded strong ground motions. The results of the nonlinear numerical analyses indicate that the model can accurately capture the torsional response of the actual structure and the concentration of damage at the south end of the first story. However, in this study, only the elastic behavior of the FE model is considered due to the low amplitude of the ambient vibration measurements. More details on the calibrated properties and the numerical model can be found in Bose et al. [56].

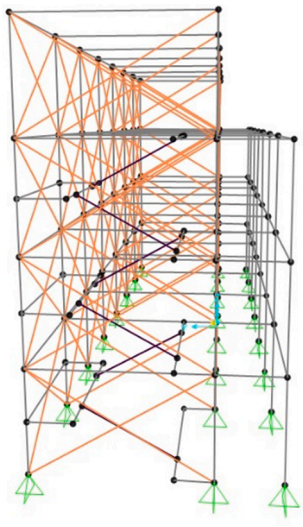

Fig. 10. 3D Model of the school building developed in OpenSEES.

The modal parameters of the undamaged structural model are calculated and compared to the identified values, as shown in the fourth column of Table 7. The natural frequencies of the initial elastic model are higher than the identified values. This is expected as the model represents the undamaged structure, while the ambient vibration data was recorded after the actual building was damaged. A more direct comparison would be achieved if the model is subjected to the strong motions caused by the earthquake sequence, and then compared to the recorded data. However, this would increase the required computational time as the nonlinear model would need to get updated, which is outside the scope of this study. Hence, the mode shapes shown in Fig. 11 are expected to be different between the undamaged model and the damaged building. However, it can be seen that the first identified mode is in excellent agreement with its model counterpart while there is some discrepancy for the second and third modes.

5. FE model updating for damage assessment

The measured ambient vibration data represent dynamic response of the building in its linear range. Therefore, only equivalent linear stiffness (modulus of elasticity) of different structural components are considered as updating parameters. The normalized updating parameters θ_i are defined as:

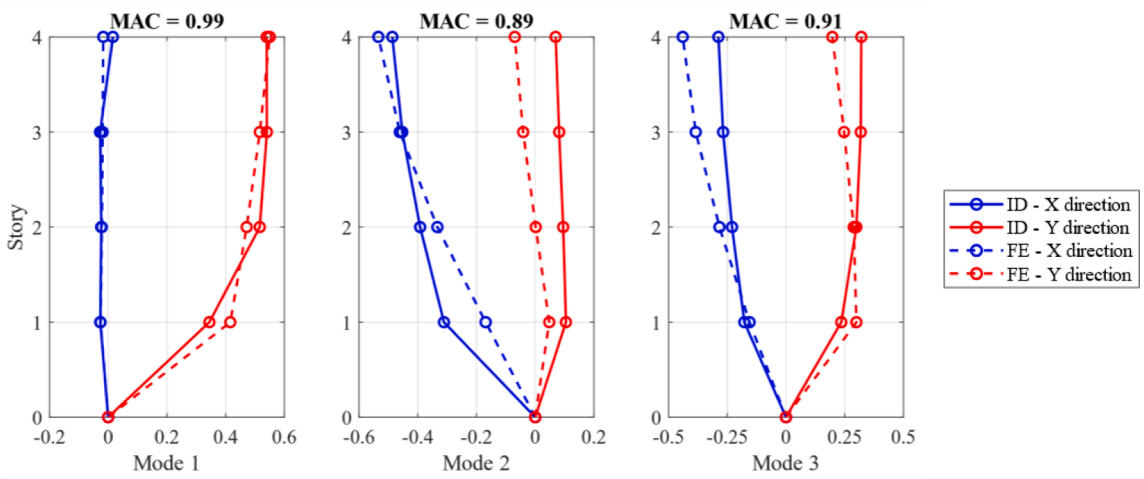

Fig. 11. Identified (ID) and initial finite element (FE) mode shapes.

$$\theta_i = \frac{E_i^{Updated}}{E_i^{Initial}} \tag{3}$$

where E_i is Young's modulus for the i^{th} group of structural components. In this study, two cases of model updating are performed, considering different parametrizations and prior assumptions. In both cases, the number of updating parameters is kept small to avoid ill-conditioning of the inverse problem. In the first case, the severely damaged elements of the first story are removed since they were judged not to have a significant remaining stiffness contribution based on the visual inspection. These elements (shown as crossed elements in Fig. 12) are identified in the surveying phase and are columns H1, H2, G1, and G2 and infill walls H12 and E12.

The considered groups of elements in the first case of model updating are the following. Columns and beams of the building are grouped together, and their stiffness is updated as parameter θ_1. In each of the first two stories, three updating parameters are chosen for masonry walls, as depicted in Fig. 12 (parameters θ_2 to θ_7). In each of the top two stories, just one updating parameter is considered to represent masonry walls, namely θ_8 for walls of the third story and θ_9 for walls of the fourth story. This selection of parameters allows investigating the stiffness changes in structural elements of interest while keeping the number of updating parameters low to avoid ill-conditioning of the inverse problem.

In the second case of model updating, a different set of updating parameters is considered for the first story of the building, including the structural elements that were removed from the initial model in Case 1. This set of parameters are selected to verify our assumption about the severity of damage in the removed elements. The prior distribution of updating parameters in Case 2, are estimated from the point cloud data. Therefore, this case combines the detected damage from point clouds (as prior PDFs) with the vibration measurements (as likelihood function) in the Bayesian model updating process. In the deterministic updating process, the detected damage from point cloud is used in the regularization term of the objective function, which is similar to the prior term in the Bayesian framework. The updating parameters include only elements of the first story, assuming that damage is concentrated in this story and changes in higher stories are negligible. The validity of this assumption is confirmed by the results of the first case of model updating. In the second case, θ_2, θ_3, and θ_4 represent walls of the first story as defined in the previous case, while θ_1 stands for walls E12 and H12 from the first story that were removed before. In this case, θ_5 and θ_6 represent columns of the first story in the northern and southern side of the building, respectively, with θ_6 including the columns removed from the first case of model updating. Fig. 13 demonstrates the considered groups of elements for each updating parameter θ_1 to θ_6. In this figure, dashed lines refer to the previously removed elements.

As previously mentioned, in Case 2 of model updating, the prior distribution of updating parameters (stiffness) is defined using the quantified damage derived from point cloud analysis. In order to quantify the prior mean stiffness values from point clouds, exponential equations have been developed based on surface defect percentage and AUC values. For the exterior walls of the first story, the following equation is used:

$$\kappa_i = \alpha_w e^{\beta_w AUC_i} \tag{4}$$

where κ_i is the stiffness ratio for individual wall *i*, defined as the ratio between the updated and initial stiffness values, and AUC_i is the AUC value for structural element *i*. The parameters α_w and β_w are coefficients of the exponential equation, estimated by assuming no loss of stiffness for the wall with the highest AUC value (CD2) and 80% loss of stiffness for the wall with the lowest AUC value (H12). These limits on the stiffness ratios, as well as the exponential pattern in stiffness reduction, are selected based on engineering judgment and are observed to have the best consistency with the visual inspection in comparison to other

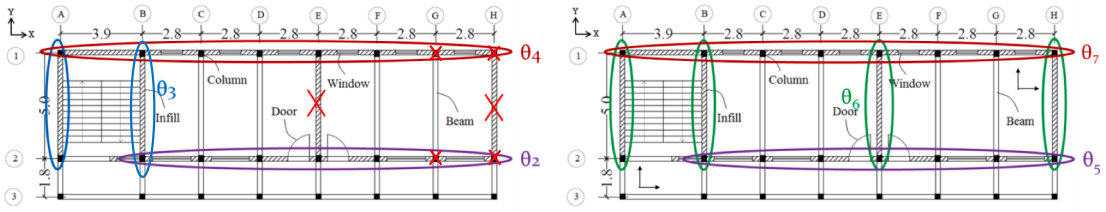

(a) Updating parameters in the 1st story **(b)** Updating parameters in the 2nd story

Fig. 12. Updating parameters for Case 1 of model updating.

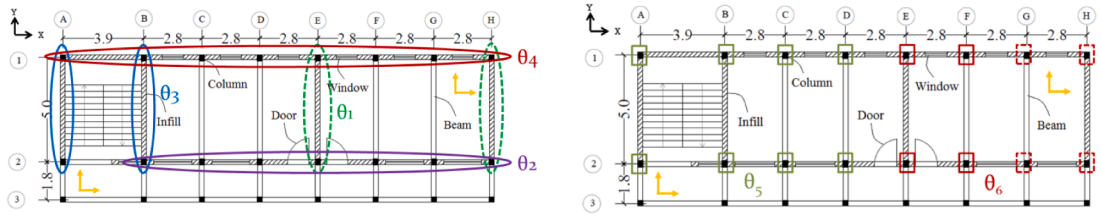

(a) Updating parameters for walls θ_1 - θ_4 **(b)** Updating parameters for columns θ_5 - θ_6

Fig. 13. Updating parameters for Case 2 of model updating.

stiffness estimation scenarios. Values of parameters α_w and β_w are reported in Table 4. The small value of α_w is caused by the exponent of large AUC_i values.

Table 5 shows the estimated mean of the prior stiffness for first-story walls. For the interior walls (B12 and E12), no AUC value was available, and therefore, their prior stiffness values are estimated based on the surface defect percentage values reported in Table 3. E12 is estimated to have an 80% loss of stiffness given that it has almost the same surface defect percentage as H12, while B12 is assumed to have no loss of stiffness since it has a very small surface defect percentage.

Based on the estimated stiffness values in Table 5, mean values for prior PDF of updating parameters θ_1, θ_2, θ_3 and θ_4 are estimated as 0.20, 0.63, 0.94 and 0.68, respectively, using the average of wall stiffness ratios in each substructure.

A similar equation is used to estimate the mean prior stiffness ratios of the first story columns using the following equation:

$$\kappa_i = \alpha_c e^{\beta_c SD_i} \tag{5}$$

where κ_i is the stiffness ratio for individual column i, SD_i represents the surface defect percentage value for the structural element i and α_c and β_c are coefficients of the exponential equation. These coefficients are calculated assuming no loss of stiffness for the columns with the lowest surface damage values (staircase columns) and assuming 80% loss of stiffness for the column with the highest surface damage value. Values of α_c and β_c for columns of the first story are also reported in Table 4. Similar to the equation proposed for walls, choice of the bounds and the exponential model for the stiffness ratios are subjective. These choices are made based on the observation that smaller values of surface defect percentage correspond to negligible loss of stiffness. However, as the surface defect percentages increase, their effect on loss of stiffness grows exponentially. A trial and error approach is implemented to choose the model form between stiffness and surface defect percentage. Table 6 summarizes the mean estimates of prior stiffness ratios for the first story columns along with the surface defect percentages. Based on the estimated stiffness ratios, the mean values for prior PDF of updating parameters θ_5 and θ_6 are estimated as 0.88 and 0.45, respectively, using the average of individual column stiffness ratios in each substructure.

While point cloud data analysis for damage detection and quantification introduces additional computational costs, this process can significantly reduce time and effort during site visits and enable inspectors to document the structural systems efficiently at a safer distance in comparison to traditional methods. Besides, the proposed damage detection and quantification methods have only a linear computational cost [44]. Lastly, using an informed prior based on the quantified damage from point cloud data reduces the computational cost of model updating process for large complicated structural systems by helping to avoid extra iterations needed to address convergence issues in the sampling process.

The proposed exponential function establishes a relationship between the quantified surface defects from point clouds and the structural stiffness for the given structure. However, further research is required to study the efficiency and accuracy of alternative stiffness-surface defect models.

Table 4
Coefficients of the exponential equation for walls and columns.

	α	β
walls	5.42e-27	0.162
columns	19.8	−0.115

Table 5
Surface defect percentage values and prior estimates of stiffness for selected columns of the first story.

Member ID	AUC (Surface Defect %)	Mean values for Prior Stiffness Ratio	Updating Parameter
H12	364.29 (22%*)	0.20	θ_1
E12	(23%*)	0.20	
EF2	364.67	0.21	θ_2
DE2	368.74	0.41	
FG2	369.89	0.49	
GH2	369.90	0.49	
AB2	373.67	0.91	
BC2	373.86	0.93	
CD2	374.26	1.0	
A12	373.51	0.88	θ_3
B12	(5%*)	1.0	
FG1	371.06	0.59	θ_4
BC1	371.93	0.68	
DE1	372.04	0.70	
AB1	372.49	0.75	

*Surface defect percentages based on Table 3.

Table 6
Surface defect percentage values and mean values for prior stiffness ratio for selected columns of the first story.

Member ID	Surface Defect (%)	Mean values for Prior Stiffness Ratio	Updating Parameter
A2	6	1.0	θ_5
B2	26	1.0	
C2	29	0.71	
D2	28	0.79	
E2	32	0.50	θ_6
F2	33	0.45	
G2	30	0.63	
H2	40	0.20	

5.1. Deterministic model updating

The deterministic model updating is formulated as a least squares problem where updating parameters are estimated by minimizing an objective function. The objective function is defined as a weighted square error between the identified and model-predicted modal parameters (natural frequencies and mode shapes) plus a regularization term.

$$f(\theta) = \mathbf{e}(\theta)^T \mathbf{W} \mathbf{e}(\theta) + (\theta - \theta_0)^T \mathbf{W}_\theta (\theta - \theta_0) \tag{6}$$

In Equation (2), $\mathbf{e}(\theta)$ is the error vector, and $\mathbf{W}$ is a diagonal matrix which specifies the weight of each modal parameter error in the objective function. The weights for natural frequencies of modes 1 to 3 are 1.0, 0.74, and 0.4, respectively. These values are inversely proportional to the variability of identified natural frequencies. The weights for mode shape components of modes 1 to 3 are 0.09, 0.07, and 0.04, respectively, which are equal to their corresponding natural frequency weights divided by the number of mode shape components (11). θ_0 is the vector of initial values for updating parameters (corresponds to the mean of prior distribution in the Bayesian approach), and $\mathbf{W}_\theta$ is a diagonal matrix of regularization weights (corresponds to the covariance matrix of prior distribution in the Bayesian approach). In this study, the regularization weights (diagonal terms of $\mathbf{W}_\theta$) are selected as 0.02. These weights indicate the degree of confidence in our initial values. Larger regularization weights would ignore the data while smaller weights allow the results to only rely on data, which is not ideal in case of having noisy data or informative prior knowledge. A relatively small weight on the prior assumption of updating parameters would allow the updating parameter to rely on data but also limit their divergence in cases where the updating parameters are not sensitive to measurements. The 0.02 value is selected after a sensitivity study of results to the regularization factor. It has been found that regularization factors in the range of 0.01 to 0.05 provide similar and reasonable results. The error vector is defined as:

$$\mathbf{e}(\theta) = \begin{bmatrix} \mathbf{e}_\omega(\theta) \\ \mathbf{e}_\Phi(\theta) \end{bmatrix} \tag{7}$$

$$\mathbf{e}_\omega(\theta) = \frac{\tilde{\omega}_m^2 - \omega_m^2(\theta)}{\tilde{\omega}_m^2} \tag{8}$$

$$\mathbf{e}_{\Phi_m} = \frac{\tilde{\Phi}_m}{\left\|\tilde{\Phi}_m\right\|} - a_m \frac{\Gamma\Phi_m(\theta)}{\|\Gamma\Phi_m(\theta)\|} \tag{9}$$

where $\mathbf{e}_\omega$ and $\mathbf{e}_\Phi$ are the eigenfrequency and mode shape error functions, $\tilde{\omega}_m = 2\pi\tilde{f}_m$ is the average identified circular natural frequency for mode m, $\tilde{\Phi}_m$ is the identified mode shape vector for the m^{th} mode, $\mathbf{\Gamma}$ is a Boolean matrix selecting the measured components of the model mode shapes and a_m is a scaling factor defined as:

$$a_m = \frac{\tilde{\Phi}_m^T \Gamma\Phi_m(\theta)}{\left\|\tilde{\Phi}_m\right\| \|\Gamma\Phi_m(\theta)\|} \tag{10}$$

The sensitivity of the objective function to updating parameters is initially confirmed through a finite difference sensitivity analysis. Fig. 14 provides the sensitivity of the objective function (normalized to one and without the regularization term) with respect to the considered updating parameters. The sensitivity plots are shown for parameters θ_1–θ_4 of Case 1 in Fig. 14a, parameters θ_5–θ_9 of Case 1 in Fig. 14b, and parameters θ_1, θ_5 and θ_6 of Case 2 in Fig. 14c. Note that parameters θ_2 to θ_4 are common in the two cases. From this figure, it is seen that the objective function is sensitive to all the considered parameters, but the levels of sensitivity differ for different parameters. At the initial values of the parameters ($\theta_i = 1$), the largest sensitivity is observed for θ_2, θ_4, θ_7, θ_8 of Case 1, and θ_1, θ_6 of Case 2. It is worth noting that the objective function shows significant sensitivity to all the parameters representing elements/components of the building with potential damage, i.e., θ_2 and θ_4 of Case 1, and θ_1 and θ_6 of Case 2. MATLAB's constrained nonlinear multivariable optimization algorithm [57] is used to find the minimum for the multivariate nonlinear objective function, with a lower bound of 0.0 and upper bound of 3.0 as the constraints.

5.2. Bayesian model updating

In addition to the deterministic model updating, a Bayesian model updating procedure is performed to find the probability distribution of updating parameters. Once the parameter distributions are estimated, the most likely values and their estimation uncertainties are reported.

The Bayes formula can be expressed as:

$$p(\theta|\mathbf{d}) = cp(\mathbf{d}|\theta)p(\theta) \tag{11}$$

where $p(\theta|\mathbf{d})$ is the posterior distribution of updating parameters given the measured data $\mathbf{d}$, (here the identified natural frequencies and mode shape components), $p(\mathbf{d}|\theta)$ is the likelihood function and reflects the probability of observing a specific set of measured data $\mathbf{d}$, for given updating parameters, $p(\theta)$ is the prior distribution based on our initial understanding of the updating parameters, and c is a normalizing constant representing the inverse of the evidence term in Bayes formulation ($p(\mathbf{d})$).

In this study, the updating parameters are assumed to be statistically independent and follow Gaussian distributions with mean θ_0 and

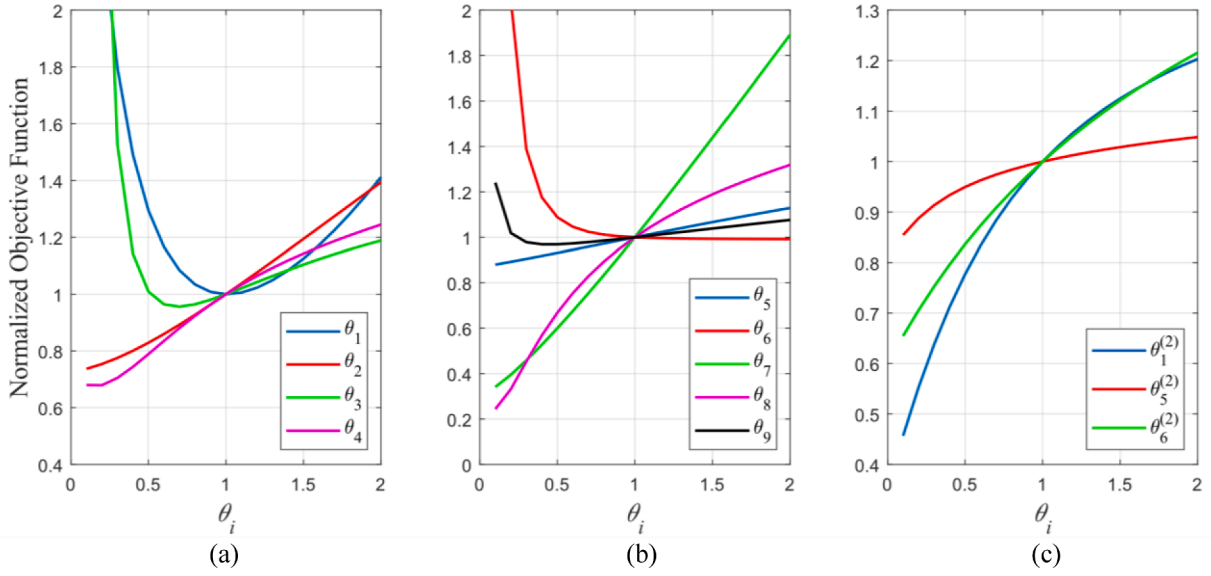

Fig. 14. Sensitivity of normalized objective function to updating parameters for both cases of updating (a and b for Case 1, and c for Case 2).

variance $\sigma_{\theta_i}^2$ for their priors. The joint prior distribution of updating parameters can be expressed as:

$$p(\theta) = \prod_{i=1}^{N_p} exp\left(-\frac{1}{2}\frac{(\theta_i - \theta_{0i})^2}{\sigma_{\theta_i}^2} \right) \quad (12)$$

where N_p is the number of updating parameters.

The error functions are defined similar to the ones in the deterministic approach and Gaussian distributions are considered for them according to the principle of maximum entropy. For a given set of model parameters $\boldsymbol{\theta}$, the likelihood of measured data will have the same distribution as the error functions, i.e., Gaussian. Assuming independency for the identified modal parameters, the likelihood function can be formulated as a product of the marginal probabilities of eigenfrequencies and mode shapes:

$$p(\mathbf{d}|\theta) = \prod_{m=1}^{N_m} p(\tilde{\omega}_m|\theta) p(\tilde{\Phi}_m|\theta) \quad (13)$$

here, N_m refers to the number of modes. Considering the prior distribution of Equation (8) and likelihood function of Equation (9), the posterior distribution can be expressed as:

$$p(\theta|\mathbf{d}) \propto exp\left(-\frac{1}{2} J(\theta, \mathbf{d}) \right) \quad (14)$$

where $J(\theta, \mathbf{d})$ is:

$$J(\theta, \mathbf{d}) = \sum_{m=1}^{N_m} \frac{e_{\omega_m}^2}{\sigma_{\omega_m}^2} + \sum_{m=1}^{N_m} \frac{\mathbf{e}_{\Phi_m}^T . \mathbf{e}_{\Phi_m}}{\sigma_{\Phi_m}^2} + \sum_{i=1}^{N_p} \frac{(\theta_i - \theta_{i_0})^2}{\sigma_{\theta_i}^2} \quad (15)$$

here, σ_{ω_m}, σ_{Φ_m} and σ_{θ_i} are standard deviations of identified eigenfrequencies, mode shapes, and the prior distribution of updating parameters, respectively. In this Equation, $\sigma_{\Phi_m}^2 = N_s \sigma_{\omega_m}^2$ with N_s representing the size of mode shapes, and σ_{θ_i}'s are chosen so that the prior term has the same weight as it has in the deterministic formulation. The Metropolis Markov Chain Monte Carlo (MCMC) algorithm [58] is used to generate 20,000 sample points of the joint posterior probability distribution of updating parameters.

5.3. Model updating results

Table 7 compares the modal parameters of the initial and updated models with the identified values for both cases of model updating. It can be seen that modal parameters for the updated models using either deterministic or Bayesian approach for both cases of updating are in excellent agreement with those identified from measured data.

Case 1 results: Table 8 reports the optimal values of updating parameter from the deterministic approach together with the most probable or *maximum a-posteriori* (MAP) values and their estimation uncertainties obtained from the Bayesian approach. It can be observed that the optimal parameter values from the deterministic approach are in good agreement with the most probable values from the Bayesian approach. This agreement verifies that the implemented sampling method, number of samples, and the proposal sampling distribution are sufficient to sample the high probability region of the posterior joint probability distribution of updating parameters. This is further validated by the close agreement between values of the objective function at the optimum parameter values in the deterministic approach and at the MAP values in the Bayesian approach.

Table 8
Updating parameter values for Case 1 from deterministic and Bayesian approaches.

Updating Parameter	Deterministic Model Updating	Bayesian Model Updating	
		MAP	Std
$\boldsymbol{\theta_1}$ (beams and columns)	1.16	1.16	*0.058*
$\boldsymbol{\theta_2}$ (1st story-western walls)	0.34	0.35	*0.059*
$\boldsymbol{\theta_3}$ (1st story-A12 and B12 walls)	0.97	0.96	*0.173*
$\boldsymbol{\theta_4}$ (1st story-eastern walls)	0.29	0.29	*0.032*
$\boldsymbol{\theta_5}$ (2nd story-western walls)	0.84	0.80	*0.101*
$\boldsymbol{\theta_6}$ (2nd story-A12, B12,E12 and H12 walls)	0.82	0.85	*0.108*
$\boldsymbol{\theta_7}$ (2nd story-eastern walls)	0.76	0.71	*0.108*
$\boldsymbol{\theta_8}$ (3rd story-walls)	0.94	0.96	*0.099*
$\boldsymbol{\theta_9}$ (4th story-walls)	1.00	0.93	*0.108*
Final Objective Function Value	6.48	6.51	

Fig. 15 shows samples from the posterior distribution of two updating parameters. In this figure, values of unnormalized posterior probability density functions are plotted versus values of parameters θ_4 (left) and θ_5 (right) for all the MCMC samples. For each value of θ_4 (or θ_5), there may be several circles providing the posterior PDF values with different combination of other parameters. While this plot is different from a marginal posterior PDF plot, it is usually informative since the MAPs and the variability with respect to one parameter can be clearly observed directly from the samples. The corresponding histograms and Kernel PDFs of these two parameters are shown in Fig. 16. Kernel PDFs, presented by the black lines, are normalized to match the highest histogram bins and the black dots represent the MAP estimates.

Case 2 results: In this case, the initial values for updating parameters (θ_0) are chosen based on the estimated values in Tables 5 and 6 to reflect the results of point cloud data analysis both in the deterministic updating (i.e., in the regularization term of equation (6)) and Bayesian updating (i.e., the prior term of equation (11)). Table 9 reports the updated values of parameters in Case 2 for the deterministic and Bayesian approaches. It can be seen that similar to Case 1, the optimal updating parameters of the deterministic approach are in close agreement with the most probable values from the Bayesian approach. The assumption of severe damage in θ_1 and θ_6 (columns and walls of the southern side of the first story) in Case 1 is confirmed with θ_1 converging almost to zero and θ_6 estimated to be as low as 0.14. The low standard deviations for these two parameters also indicate a high level of confidence in the estimation. It should be noted that the updated values of θ_2 and θ_4 (eastern and western walls of the 1st story), which were defined similarly in the two cases, are consistently reduced in both cases, which confirms the loss of stiffness at these locations. Compared to Case 1, the

Table 7
Modal parameters of reference and calibrated models together with identified values for the first case of model updating.

Modal Parameters	Mode	System Identification	Model of Undamaged Building	Case 1		Case 2	
				Deterministic Model Updating	Bayesian Model Updating	Deterministic Model Updating	Bayesian Model Updating
Frequencies (Hz)	1	1.19	1.30	1.19	1.20	1.20	1.20
	2	2.16	2.69	2.17	2.16	2.16	2.16
	3	3.16	3.39	3.15	3.14	3.14	3.15
MAC Values	1	–	0.99	0.99	0.99	0.99	0.99
	2	–	0.89	0.99	0.99	1.00	0.99
	3	–	0.91	0.98	0.98	0.99	0.99

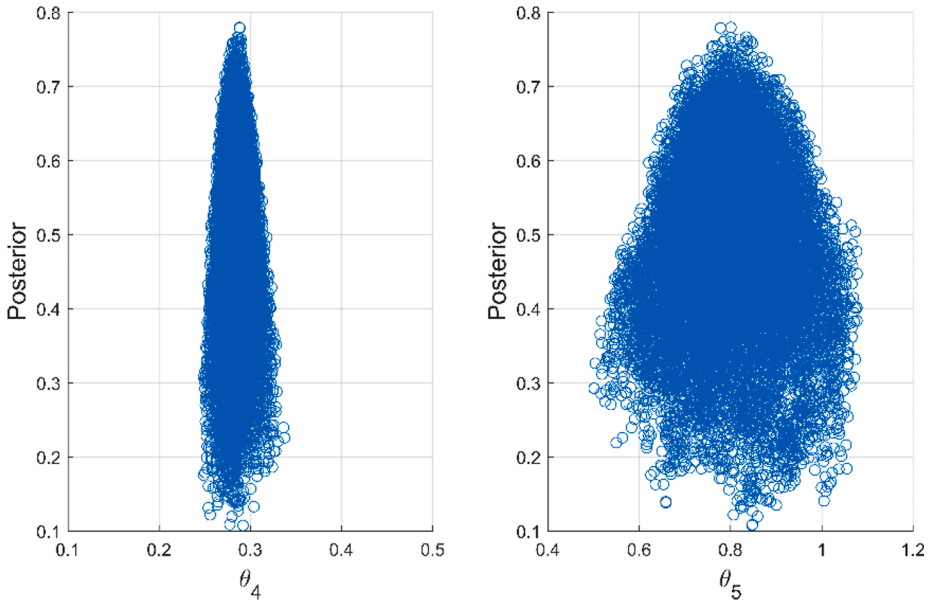

Fig. 15. Distribution of sampled parameters versus the unnormalized posterior probability densities for updating parameters θ_4 and θ_5.

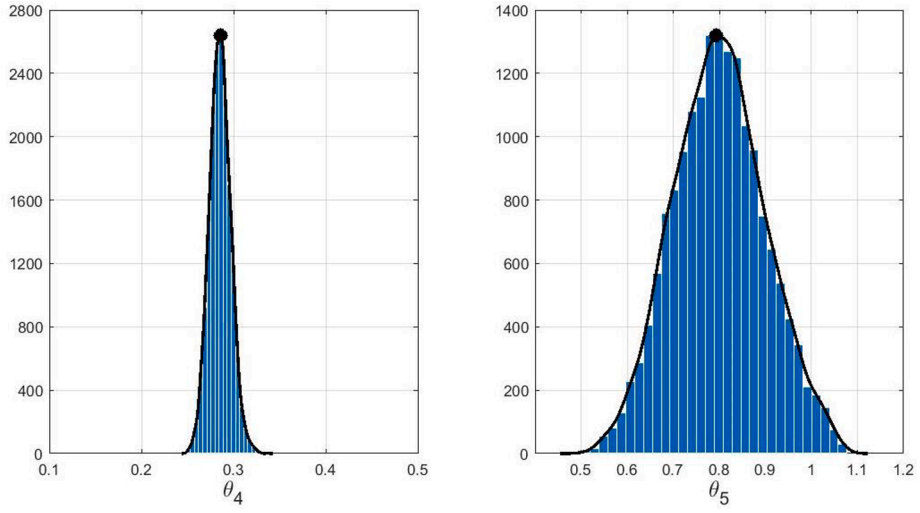

Fig. 16. Histogram and kernel PDF for posterior probability of updating parameters θ_4 and θ_5.

Table 9
Updating parameter values for Case 2 from deterministic and Bayesian approaches.

Updating Parameter	Deterministic Model Updating	Bayesian Model Updating	
		MAP	Std
$\boldsymbol{\theta_1}$ (1st story-walls E12 and H12)	0.0007	0.0012	*0.0009*
$\boldsymbol{\theta_2}$ (1st story-western walls)	0.17	0.17	*0.039*
$\boldsymbol{\theta_3}$ (1st story-walls A12 and B12)	0.93	0.91	*0.097*
$\boldsymbol{\theta_4}$ (1st story-eastern walls)	0.28	0.29	*0.023*
$\boldsymbol{\theta_5}$ (1st story-Northern columns)	0.97	0.95	*0.031*
$\boldsymbol{\theta_6}$ (1st story-Southern columns)	0.14	0.15	*0.005*
Final Objective Function Value	*4.72*	*4.77*	

Bayesian approach for this case provides lower standard deviations for updated parameters indicating higher sensitivity of lower story structural components to the vibration data and therefore better inference of these parameters.

Comparison with LIDAR results: The point cloud data were analyzed using two metrics, including percent of surface defect for columns and interior walls and AUC for exterior masonry walls. As presented, the percentage of damage computed for walls E12 and H12 were approximately 4 times higher than that of B12 wall, based on the interior scans analysis result, which reveals a similar pattern to those computed for Bayesian and deterministic model updating parameters of the two walls. A similar pattern was also observed based on the computed AUC of the exterior walls where the mean values of AUC for the western walls were lower than that of mean AUC values computed for the eastern walls. In addition, the computed surface defect percentages for the columns on the northwestern and southwestern sides of the structures show a similar pattern for model updating parameters. Lastly, the point cloud analysis results for columns H2 and G2 and walls H12 and E12 demonstrate that these elements sustained significant damage in comparison to other

similar elements within the structure.

6. Model prediction considering modeling errors

In this section, the calibrated model from the first model updating case is used to probabilistically predict the response (natural frequencies here) of the building. Previous studies have shown that considering just the updated structural parameter values may not be sufficient for accurate model predictions due to the effect of modeling errors [16,59,60]. In order to provide more realistic predictions of natural frequencies, modeling error is also added to the response prediction process. Using the error function of Equation (4), natural frequency of mode m can then be estimated as:

$$\left(\omega_m^{estimate}\right)^2 = \frac{\omega_m^2(\theta)}{1-\mathbf{e}_{\omega_m}} \tag{16}$$

As previously mentioned, the natural frequency errors are modeled as a set of uncorrelated zero-mean Gaussian distributions with variance $\hat{\sigma}^2_{\omega_m}$:

$$\hat{\sigma}^2_{\omega_m} = \frac{\sum_{t=1}^{N_t} \hat{e}^2_{\omega_m}}{N_t - 1} \tag{17}$$

where N_t is the number of available data sets.

For probabilistic response prediction, 200 sets of model parameter values are selected based on the posterior distributions of section 5.3. Natural frequencies are estimated with and without considering the modeling error term. These two sets of predictions are plotted in Fig. 17 together with the measurements (identified natural frequencies). This figure shows the natural frequency predictions pairwise, with the lower diagonal subplots showing predictions without considering error while upper diagonal subplots include the error in predictions. It can be seen that including the error term provides more realistic confidence bound for the prediction as the upper diagonal subplots contain most of the measured natural frequencies while the lower diagonal subplots provide inaccurate uncertainty bounds. Therefore, it is highly recommended to account for the effects of modeling errors even after updating to provide realistic confidence bounds on model predictions [61].

7. Summary and conclusions

The paper investigates the extent of post-earthquake structural damage in an RC infilled frame school building. Finite element model updating using ambient acceleration data, and point clouds is implemented for this purpose. Two cases of model updating are performed with different sets of updating parameters. In Case 1, all structural elements, with the exception of those visually observed to be severely damaged, are modeled and updated. In Case 2, all structural elements of the first story, including the severely damaged elements, are updated while their prior stiffness values are estimated from the point cloud measurements. It is confirmed that the elements with clear visual damage have little remaining stiffness. In the model updating process, deterministic and Bayesian approaches are deployed. Optimum parameter values from the deterministic approach are in good agreement with the MAP estimates obtained from the Bayesian approach for both cases of updating. The Bayesian updating results indicate higher confidence (lower standard deviation) for the severely damaged elements for both cases. Collected point cloud data are also used to quantify the observable surface defects. A set of interior and exterior point clouds are used to estimate the relative surface damage of the columns, and exterior and interior walls of the first story. The estimated surface defect metrics are in good agreement with the observed damage as well as model updating results. Case 2 of model updating shows a successful application of a model updating process in which point clouds and vibration measurements are combined in a Bayesian inference approach. The addition of point cloud analysis improves the results by providing more realistic prior distributions, which makes the stochastic sampling

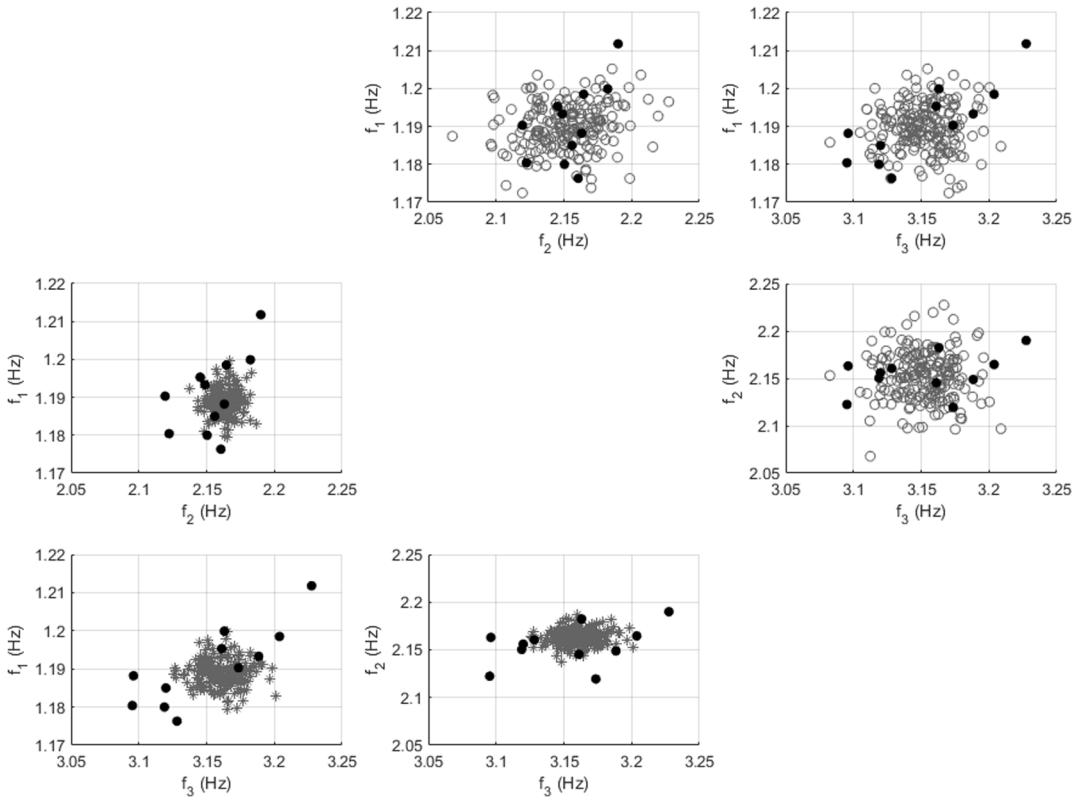

Fig. 17. Model calculated vs. identified natural frequencies with and without accounting for modeling errors; black circles are identified, grey stars are predicted without considering modeling errors, and grey circles are predicted considering modeling errors.

approach more efficient and avoids un-identifiability. A more objective process for selecting the prior distribution of updating parameters reduces the estimation uncertainty and allows including the severely damaged components in the updating process. It is worth noting that the proposed relationship between the point cloud analysis results and prior stiffness distributions may not be generally applicable; however, the focus of this study is to explore the viability of such an approach. These surface defect vs. stiffness relationships can be fine-tuned in future studies considering additional data. Finally, the calibrated model is used for response (natural frequency) prediction of the building. The effects of modeling error in the prediction process are studied, and it is found that adding the modeling error term will significantly improve the prediction results. Therefore, it is strongly recommended to account for modeling errors in addition to the model parameter uncertainties obtained from Bayesian model updating to achieve realistic confidence bounds on model predictions.

CRediT authorship contribution statement

Mehdi M. Akhlaghi: Conceptualization, Methodology, Software, Formal analysis, Writing - original draft, Visualization. **Supratik Bose:** Methodology, Software, Validation. **M. Ebrahim Mohammadi:** Methodology, Software, Visualization. **Babak Moaveni:** Conceptualization, Supervision, Funding acquisition. **Andreas Stavridis:** Conceptualization, Investigation, Funding acquisition. **Richard L. Wood:** Conceptualization, Investigation, Funding acquisition.

Declaration of Competing Interest

The authors declared that there is no conflict of interest.

Acknowledgments

Partial support of this study by the National Science Foundation Grants 1903972 and 1545595 is gratefully acknowledged. The opinions, findings, and conclusions expressed in this paper are those of the authors and do not necessarily represent the views of the sponsors and organizations involved in this project.

References

[1] Kamat VR, El-Tawil S. Evaluation of augmented reality for rapid assessment of earthquake-induced building damage. J. Comput. Civ. Eng. 2007;21:303–10.
[2] Huang CS, Hung SL, Wen CM, Tu TT. A neural network approach for structural identification and diagnosis of a building from seismic response data. Earthq. Eng. Struct. Dyn. 2003;32:187–206.
[3] Moaveni B, Conte JP, Hemez FM. Uncertainty and sensitivity analysis of damage identification results obtained using finite element model updating. Comput. Civ. Infrastruct. Eng. 2009;24:320–34.
[4] Mottershead JE, Link M, Friswell MI. The sensitivity method in finite element model updating: a tutorial. Mech. Syst. Signal Process. 2011;25:2275–96.
[5] Friswell MI, Mottershead JE. Finite Element Model Updating in Structural Dynamics. Boston; Dordrecht: Kluwer Academic Publishers; 1995.
[6] Sohn H, Farrar CR, Hemez FM, Shunk DD, Stinemates DW, Nadler BR. A review on structural health monitoring literature. 1996–2001, Cambridge: Los Alamos National Laboratory; 2003. Technical Report annex to SAMCO summer academy.
[7] Carden EP, Fanning P. Vibration Based Condition Monitoring: A Review. Structural Health Monitoring 2004;3(4):355–77.
[8] Salawu OS. Detection of structural damage through changes in frequency: a review. Eng Struct 1997;19(9):718–23.
[9] Bicanic N, Chen H-P. Damage identification in framed structures using natural frequencies. Int. J. Numer. Meth. Engng. 1997;40(23):4451–68.
[10] Shi ZY, Law SS, Zhang LM. Damage localization by directly using incomplete mode shapes. J Eng Mech 2000;126:656–60.
[11] Lee JJ, Lee JW, Yi JH, Yun CB, Jung HY. Neural networks-based damage detection for bridges considering errors in baseline finite element models. J Sound Vib 2005;280(3-5):555–78.
[12] Pandey AK, Biswas M, Samman MM. Damage detection from changes in curvature mode shapes. J Sound Vib 1991;145(2):321–32.
[13] Pandey AK, Biswas M. Damage detection in structures using changes in flexibility. J Sound Vib 1994;169:3–17.
[14] Teughels A, De Roeck G. Structural damage identification of the highway bridge Z24 by FE model updating. J Sound Vib 2004;278(3):589–610.
[15] Sohn H, Law KH. A Bayesian probabilistic approach for structure damage detection. Earthq. Eng. Struct. Dyn. 1997;26:1259–81.
[16] Beck JL, Katafygiotis LS. Updating Models and Their Uncertainties. I: Bayesian Statistical Framework. J Eng Mech 1998;124:455–61.
[17] Ching J, Beck JL. New Bayesian model updating algorithm applied to a structural health monitoring benchmark. Struct. Heal. Monit. 2004;3:313–32.
[18] Yuen KV, Beck JL, Au SK. Structural damage detection and assessment by adaptive Markov chain Monte Carlo simulation. Struct. Control Heal. Monit. 2004;11:327–47.
[19] Ching J, Chen Y-C. Transitional markov chain monte carlo method for bayesian model updating, model class selection, and model averaging. J Eng Mech 2007;133(7):816–32.
[20] Zhang EL, Feissel P, Antoni J. A comprehensive Bayesian approach for model updating and quantification of modeling errors. Probabilistic Eng. Mech. 2011;26:550–60.
[21] Sankararaman S, Mahadevan S. Bayesian methodology for diagnosis uncertainty quantification and health monitoring. Struct. Control Health Monit. 2013;20:88–106.
[22] Behmanesh I, Moaveni B. Probabilistic identification of simulated damage on the dowling hall footbridge through Bayesian finite element model updating. Struct. Control Heal. Monit. 2015;22:463–83.
[23] Jang J, Smyth A. Bayesian model updating of a full-scale finite element model with sensitivity-based clustering. Struct Control Health Monit. 2017;24:2004.
[24] Sun H, Betti R. A hybrid optimization algorithm with bayesian inference for probabilistic model updating. Comput-Aided Civ Infrastruct Eng 2015;30:602–19.
[25] Song M, Renson L, Noël J-P, Moaveni B, Kerschen G. Bayesian model updating of nonlinear systems using nonlinear normal modes. Struct Control Health Monit. 2018;25:2258.
[26] Chatzi EN, Smyth AW. The unscented Kalman filter and particle filter methods for nonlinear structural system identification with non-collocated heterogeneous sensing. Structural Control and Health Monitoring 2009;16:99–123.
[27] Erazo K, Hernandez EM. Uncertainty quantification of state estimation in nonlinear structural systems with application to seismic response in buildings. ASCE-ASME Journal of Risk and Uncertainty in Engineering Systems, Part A: Civil Engineering 2015;2:B5015001.
[28] Wu M, Smyth AW. Application of the unscented Kalman filter for real-time nonlinear structural system identification. Structural Control and Health Monitoring 2007;14:971–90.
[29] Ebrahimian H, Astroza R, Conte JP. Extended Kalman filter for material parameter estimation in nonlinear structural finite element models using direct differentiation method. Earthquake Eng Struct Dyn 2015;44:1495–522.
[30] Erazo K, Moaveni B, Nagarajaiah S. Bayesian seismic strong-motion response and damage estimation with application to a full-scale seven story shear wall structure. Eng Struct 2019;186:146–60.
[31] Brando G, Rapone D, Spacone E, Barbosa A, Olsen M, Gillins D, et al. Reconnaissance report on the 2015 Gorkha earthquake effects in Nepal. XVI ANIDIS: L'AQUILA, Italy; 2015.
[32] Rai DC, Singhal V, Raj BS, Sagar L. Reconnaissance of the effects of the M7.8 Gorkha (Nepal) earthquake of April 25, 2015. Journal of Geomatics, Natural Hazards and Risk, Taylor and Francis 2015;7:1-17.
[33] Bose S, Martin J, Stavridis A. Simulation Framework for Infilled RC Frames Subjected to Seismic Loads. Earthquake Spectra; 2019. p. 1739–62.
[34] Bose S. Analytical and Numerical Framework for the Seismic Assessment of Infilled RC Frames. PhD Dissertation. State University of New York at Buffalo; 2019.
[35] Oppenheim AV, Willsky AS, Young IT. Signals and Systems, Englewood Cliffs. New Jersey: Prentice-Hall Inc.; 1983.
[36] Farrar CR, James III GH. System Identification from Ambient Vibration Measurements on a Bridge. J Sound Vib 1997;205:1–18.
[37] Caicedo JM, Dyke SJ, Johnson EA. Natural Excitation Technique and Eigensystem Realization Algorithm for Phase I of the IASC-ASCE Benchmark Problem: Simulated Data. J Eng Mech 2004;130:49–60.
[38] Juang JN, Pappa RS. An eigensystem realization algorithm for modal parameter identification and model reduction. Journal of Guidance, Control, and Dynamics 1985;8:620–7.
[39] Akhlaghi MM, Bose S, Moaveni B, Stavridis A. Bayesian Model Updating of a Damaged School Building in Sankhu, Nepal. Model Validation and Uncertainty Quantification 2019;3.
[40] Olsen MJ, Kayen R. Post-earthquake and tsunami 3D laser scanning forensic investigations, in Proceedings of ASCE Forensic Engineering. San Francisco: CA; 2012. p. 477–86.
[41] Guldur Erkal B, Hajjar JF. Laser-based surface damage detection and quantification using predicted surface properties. Autom Constr 2017;83:285–302.
[42] Valença J, Puente I, Júlio E, González-Jorge H, Arias-Sánchez P. Assessment of cracks on concrete bridges using image processing supported by laser scanning survey. Constr Build Mater 2017;146:668–78.
[43] Davoudi R, Miller GR, Kutz JN. Structural load estimation using machine vision and surface crack patterns for shear-critical RC beams and slabs. J Comput Civil Eng 2018;32(4):04018024.
[44] Mohammadi ME, Wood RL, Wittich CE. Non-temporal point cloud analysis for surface damage in civil structures. International Journal of Geo-Information 2019;8(12):527.
[45] Bose S, Nozari A, Mohammadi ME, Stavridis A, Moaveni B, Wood R, Gillins D, Barbosa A. Structural Assessment of a school building in Sankhu, Nepal damaged due to torsional response during the 2015 Gorkha earthquake. Proceedings of International Modal Analysis Conference, 34th IMAC, Orlando, Florida; 2016.

[46] Song M, Yousefianmoghadam S, Mohammadi ME, Moaveni B, Stavridis A, Wood RL. An application of finite element model updating for damage assessment of a two-story reinforced concrete building and comparison with lidar. Struct. Heal. Monit. 2018;17:1129–50.
[47] Pauly M, Gross M, Kobbelt L. P., Efficient simplification of point-sampled surfaces, IEEE Visualization, 2002. VIS 2002., Boston, MA, USA, 2002, pp. 163-170.
[48] McKenna F, Fenves GL, Scott MH, Jeremic B. Open system for earthquake engineering Simulation (Opensees). Pacific Earthquake Engineering Research Center: University of California, Berkeley, CA; 2000.
[49] Pradhan PL. Composite actions of brick infill wall in RC frame under in-plane lateral load. PhD Dissertation, Tribhuvan University, Pulchowk Campus 2009.
[50] ACI. 369. Guide for Seismic Rehabilitation of Existing Concrete Frame Buildings and Commentary. American Concrete Institute 2011.
[51] Bose S, Tempestti JM, Stavridis A. Simulation Framework for Infilled RC Frames Subjected to Seismic Loads. Earthquake Spectra 2019;35(4):1739–52.
[52] Spacone E, Filippou FC, Taucer FF. Fibre beam-column model for nonlinear analysis of R/C frames: Part I. Formulation, Earthquake Engineering and Structural Dynamics 1996;25:711–25.
[53] Martin J., and Stavridis, A., 2017. Simplified method to assess lateral resistance of infilled reinforced concrete frames. 16th World Conference on Earthquake Engineering, Santiago, Chile.
[54] Stavridis A, Martin J, Bose S. Updating the ASCE 41 provisions for Infilled RC frames. Proc. 2017 SEAOC Convention, San Diego, California; 2017.
[55] American Society of Civil Engineers. Seismic Evaluation and Retrofit of Existing Buildings (41-17); 2017.
[56] Bose S, Nozari A, Stavridis A, Moaveni B. Nonlinear modeling of a school at Sankhu for performance assessment during the 2015 Nepal earthquake, 16th World Conference on Earthquake Engineering. Chile: Santiago; 2017.
[57] MATLAB R2019a, MathWorks Inc., MA, USA; 2019.
[58] Metropolis N, Rosenbluth A, Rosenbluth M, Teller M, Teller E. Equations of State Calculations by Fast Computing Machines. J Chem Phys 1953;21:1087–92.
[59] Haukaas T, Gardoni P. Model uncertainty in finite-element analysis: Bayesian finite elements. J Eng Mech 2011;137:519–26.
[60] Goller B, Schueller G. Investigation of model uncertainties in Bayesian structural model updating. J Sound Vib 2011;330:6122–36.
[61] Song M, Behmanesh I, Moaveni B, Papadimitriou C. Modeling error estimation and response prediction of a 10-story building model through a hierarchical Bayesian model updating framework. Front. Built Environ. 2019;5.